A numerical finite element study on connections of SFRC offshore wind towers with prestressed CFRP reinforcement and steel connectors

Chandan C. Gowda[1*], Fabio P. Figueiredo[2], Joaquim A. O. Barros[3] and A. Ventura-Gouveia[4]

Email: chandu627@gmail.com[1], f.figueiredo@civil.uminho.pt[2], barros@civil.uminho.pt[3], ventura@estgv.ipv.pt[4]

(1) *Researcher, University of Minho, Guimarães, Portugal (*corresponding author)*
(2) *Researcher, University of Minho, Guimarães, Portugal*
(3) *Professor, University of Minho, Guimarães, Portugal*
(4) *Professor, Polytechnic Institute of Viseu, Portugal*

Abstract

The growing need for sustainable production of electricity highlights the importance and the necessity of having higher number and more effective offshore wind towers. The rapid growth of offshore wind towers is estimated to produce 4% of electricity demands in Europe by the end of 2020. The research described in this paper is part of a project dedicated for the development of innovative structural system using advanced materials for lightweight and durable offshore towers. Specifically, it discusses the nonlinear finite element modelling of the connection between representative prefabricated rings of offshore wind tower made by steel fibre reinforced concrete (SFRC), and prestressed by a hybrid system of carbon fibre reinforced polymers (CFRP) bars and steel strands. This connection is assured by post-tension high steel strength cables and concrete-concrete shear friction width an idealized geometric configuration of the faces in contact. The model takes into account the loads from the rotor, wind and water currents, by considering the critical loading conditions for the safety verifications of serviceability and ultimate limit states. The material nonlinear analyses are carried out with FEMIX V4.0 software, considering a 3D constitutive model capable of simulating the relevant nonlinear features of the SFRC, and interface finite elements for modelling the shear friction of the concrete-concrete surfaces in contact. The parametric analyses involve the influence on the relevant results of the SFRC fracture parameters, pre-stress level of the reinforcements, shape of interlock mechanism, friction angle and interface cohesion.

Keywords: Offshore wind tower; material nonlinear analyses; shear frictional and tied connections.

1. Introduction

The developing need of energy production is draining the natural resources like oil, natural gas, coal etc., at a more rapid rate than ever. This pushes the humankind to produce more sustainable energy production for the future. Offshore wind tower, which uses the powerful wind, is one these sustainable solution to produce electricity. The first wind farm was installed in Denmark in 1991 [1]. 84% of all offshore wind installations are located in European waters, with remaining 16% mainly in China, followed by Vietnam, Japan, South Korea, U.S and Taiwan [2].

Fig. 1 shows the global cumulative offshore wind capacity in 2017, which indicates that the production capacity has increased over 450% from 2011 to 2017 and is continuously growing. This moves the society towards a more productive, cost-efficient, sustainable and renewable

1

45 energy production, reducing the carbon dioxide emissions. One of the steps in reducing these
46 costs is by developing innovative structural systems, which is the main aim of the current
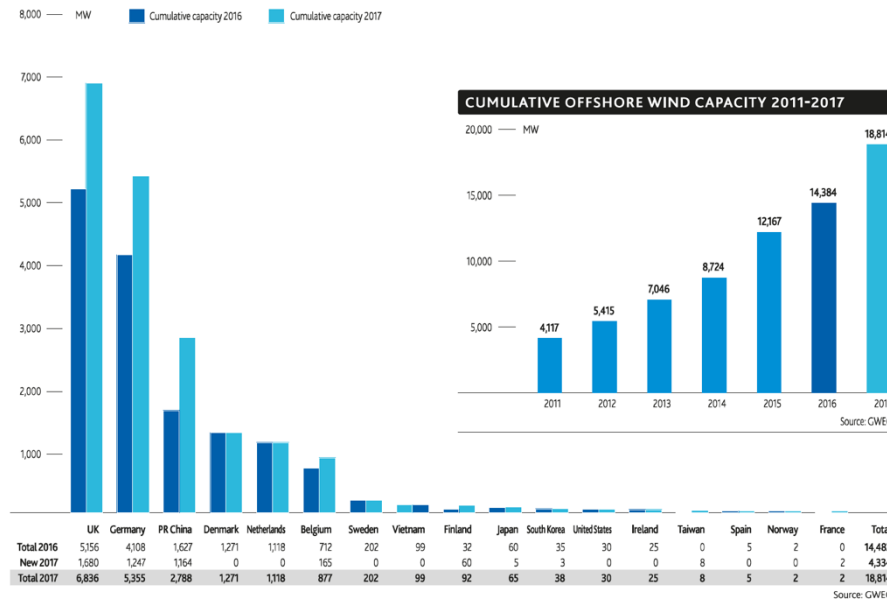47 research.

48   Fig. 1. Global cumulative offshore wind capacity in 2017 [2]

49 The proposed steel fibre reinforced concrete (SFRC) towers involve prefabricated concrete
50 rings of high dimensions assembled on site by post-tensioned steel cables. Minor changes in
51 design or construction process can have significant impact on these type of constructions in
52 terms of cost and schedule savings [3]. The innovative use of composite materials in
53 construction i.e., in support structures and foundations, will reduce fabrication and
54 transportation efforts, resulting in the most cost effective solutions [4].
55 The main scope of this paper is to perform material nonlinear analysis of the connection
56 between two representative steel fibre reinforced concrete (SFRC) prefabricated rings (of thin
57 wall and variable diameter) of the structural system developed in the scope of the research
58 project. The steel fibre reinforcement aims to eliminate the conventional steel bars, reducing
59 the ring's wall thickness. These rings are prestressed with carbon fibre reinforced polymer
60 (CFRP) bars, taking advantage of the non-corrosiveness of CFRP, while post-tensioned steel
61 cables ensure the connection between consecutive rings, providing simple, fast assembling and
62 disassembling process in the tower's construction. However, high stress gradients are expected
63 to occur in these anchoring zones, a concern that promoted the development of the present
64 material nonlinear analysis.
65

2. Simplified design approach

67 A simplified approach for the design of offshore wind towers is adopted in this paper. The
68 loads considered herein consist of forces acting on top of the structure due to wind passing
69 throughout the rotor, wind pressure on the tower structure, waves slamming the tower, and
70 loads produced by water currents on the tower structure (see Fig. 2).
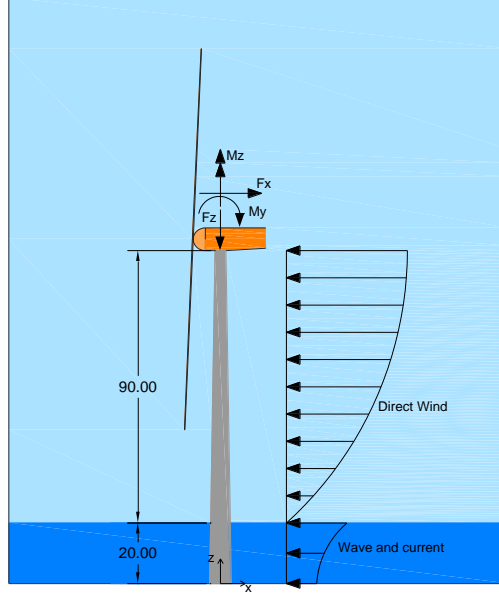
Fig. 2. Applied loads (dimensions in m).

Since it was not possible to obtain precise information about loads from turbine wind tower manufacturers, they were extrapolated from a 3 MW wind turbine [5] and are presented in Table 1. The axial forces acting on the tower are the prestressing and gravitational loads. The wind load per unit of length, f_{wi} [N/m], was calculated using the following equation:

$$f_{wi}(z) = 0.5 \, C_a \, \rho_{air} \, D(z) \, u(z)^2 \tag{1}$$

where ρ_{air} [kg/m^3] is the density of air, C_a [-] is the aerodynamic drag coefficient (shape, surface dependent), $D(z)$ [m] is the diameter of the tower cross-section at elevation z, and $u(z)$ [m/s] is the mean wind speed at elevation z. The wave and current loads were obtained using the semi-empirical Morison's equation:

$$f_M(z) = f_i(z) + f_d(z) \tag{2}$$

where $f_i(z)$ represents the hydrodynamic inertial load [N/m] and $f_d(z)$ is the hydrodynamic drag load [N/m]. A simplified approach for the design of offshore wind towers is adopted in this paper. The loads considered consist of forces acting on top of the structure due to wind passing throughout the rotor, wind pressure on the tower structure, waves slamming the tower, and loads produced by water currents on the tower structure. The paper presents the final equations used to determine the loads acting in the structure. However, it does not explain the equations in details. Detailed information about the simplified approach can be found in [6].

Table 1. Five MW wind turbine loads for serviceability and ultimate limit states (SLS, ULS).

Parameter	SLS	ULS
Horizontal shear force F_x (kN)	690	1585
Moment M_y (kN m)	1600	3677
Torque M_z (kN m)	1010	1789

Design offshore wind towers in compliance with standards requires that the structure shall satisfy ultimate, accidental, fatigue and serviceability limit state design conditions (ULS, ALS, FLS and SLS), respectively [7]. However, in this study, only the most unfavourable

3

96 combination for the ULS is considered. The load combination given by DNV [7] is calculated
97 using the following expression:

$$F = 1.0\,G + 1.35\,E \qquad (3)$$

100 where G are the permanent loads (tower, rotor and nacelle self-weight) and E are the
101 environment loads (wind, waves and currents).

3. Model

3.1. Geometry and data

105 The global height of the current tower is 110 meters, with 90 m above and 20 m below the sea
106 level. The external radius of the ring at z=0 m height (sea bed) is 3.6 meters, which reduces to
107 1.8 m (at z=110 m height) at the top. The full tower consists of 10 rings, each of 11 meters
108 high. The connection between consecutive SFRC rings is assured by post-tensioned steel
109 cables. The cross section of this connection is subjected to loads and moments generated by
110 the loading conditions described in previous section, and the global analysis is discussed
111 elsewhere [8]. According to the global analysis, the bottom most ring (z=0-11m), is subjected
112 to most unfavourable loading conditions for design purpose. As a result, the connection
113 between the bottom two rings shown in Fig. 3 i.e., the ring resting on the sea bed and the one
114 above, is analysed and the results are discussed in this paper.

| (a) | (b) |
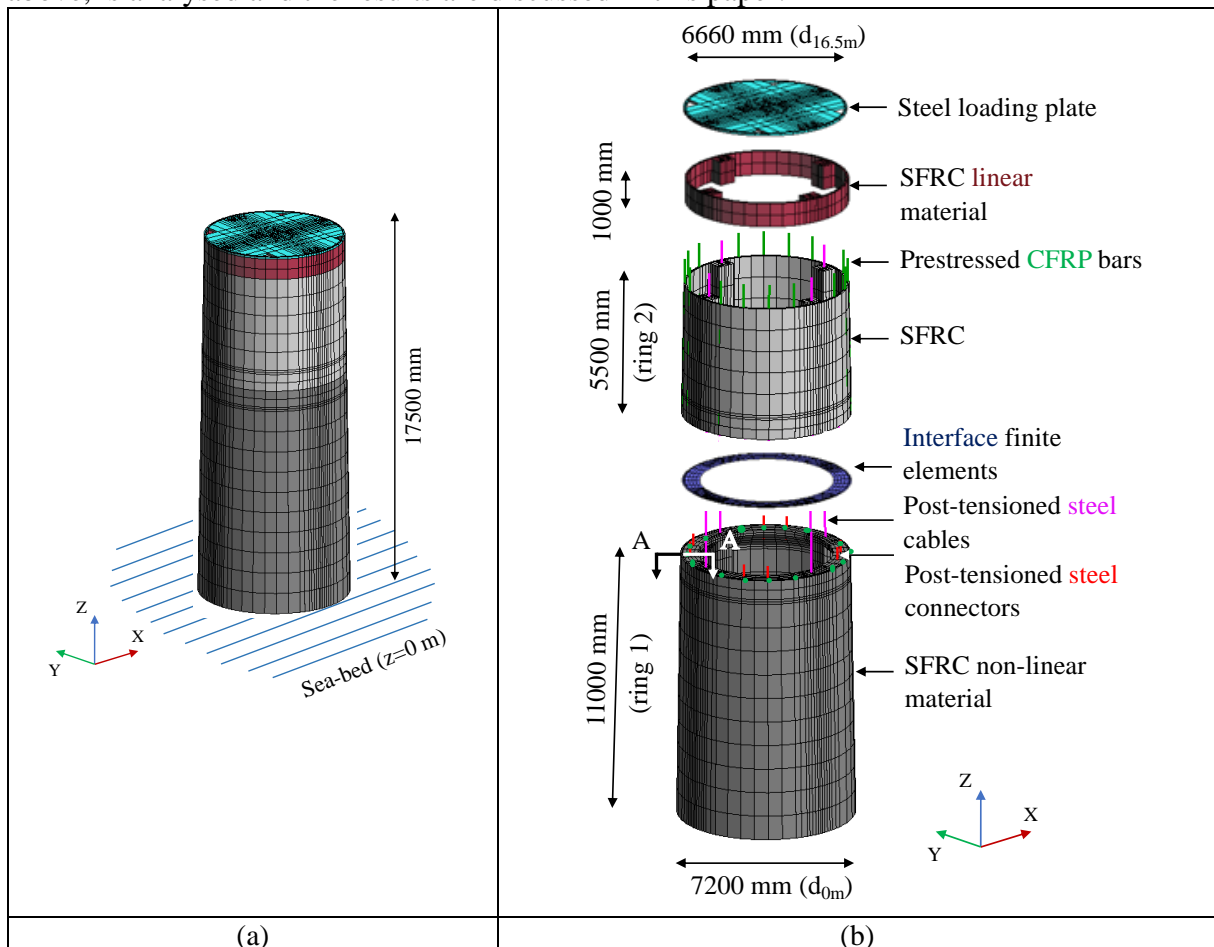
115 Fig. 3. Model "t_s1": (a) Full model and (b) Components of the model.

116 The FE model consists of the bottom full ring (11 m) and half of the ring above (5.5 m), with
117 a total height of 16.5 m (Fig. 3). The radius at the base of the tower is 3.60 m and the radius at
118 16.5 m height is 3.33 m. Excluding the four longitudinal ribs ($730\times600mm^2$ cross section, Fig.
119 3b) and the circumferential rib that assures the connection between consecutive rings, the wall
120 thickness is 100 mm. The cross section of the circumferential rib has the geometry shown in
121 Fig. 4. The connection is assured by 4 post-tensioned steel cables (one per each longitudinal
122 rib) with pre-stress level of 60% and 8 post-tensioned steel connectors distributed along the
123 perimeter of the circumferential rib with pre-stress level of 60% (see Fig. 3b). The surface of
124 connection is inclined on both the top and the bottom rings to provide additional shear
125 resistance, shown in Fig. 4. Each ring is prestressed with 16 carbon fibre reinforced polymer
126 (CFRP) bars of 30 mm diameter placed in the centre of the SFRC wall (Fig. 3b).
127

128 **3.2. FEM attributes and material properties for the constitutive model**
129 A 3D multidirectional smeared crack model [9] available in FEMIX 4.0 is used for the
130 numerical simulations. GiD software is used as a pre- and post-processor.
131

(a)   (b)
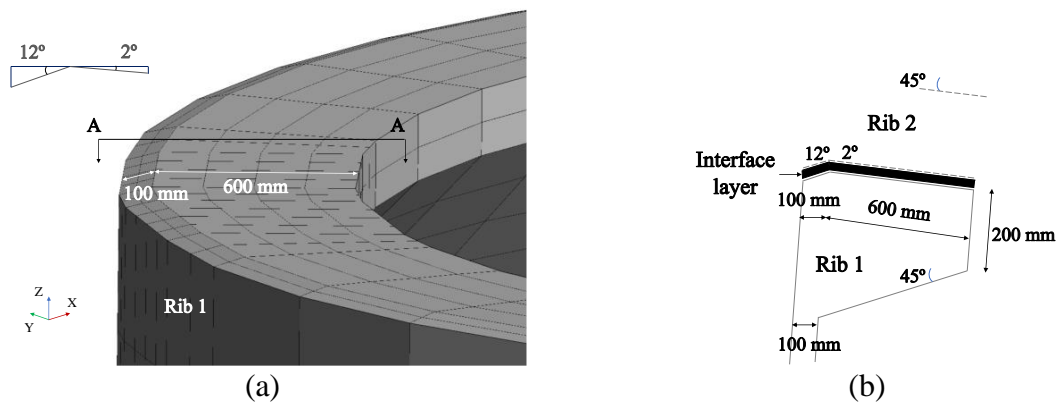
132 Fig. 4. Geometry of the circumferential rib connecting two rings: (a) 3D and (b) 2D, cross section AA.
133

134 Solid hexahedra FE of 8 nodes are used to simulate the SFRC, with $2\times2\times2$ Gauss Legendre
135 integration scheme. A maximum of 2 cracks is allowed to form at each integration point, with
136 a threshold angle of 30 degrees for the new crack formation (2nd crack). For assuring the results
137 to be independent of the FE mesh refinement, a crack bandwidth equal to the cubic root of the
138 volume of the integration point (IP), is adopted. The crack shear stress transfer is simulated
139 through incremental approach. The CFRP bars and steel cables are modelled with 2-noded 3D
140 embedded FE cable (with perfect bond). Interface finite elements of 8 nodes with 2×2 Gauss-
141 Lobato integration scheme are adopted to model the concrete-concrete contact between
142 consecutive SFRC rings (ring 1 and ring 2). An additional linear layer of SFRC (1 m thick) is
143 modelled (Fig. 3b) to avoid the development of unrealistic stress fields and severe cracking on
144 the SFRC rings, where the real tower equivalent loads are applied (top of ring 2). Furthermore,
145 a stiff steel plate is also connected to this extra linear-elastic SFRC layer to receive the
146 equivalent loads and to transfer them on the tower.
147 According to technical data sheet of the products, the adopted steel cables and connectors have
148 40 mm diameter, yield strength of 1147 MPa and modulus of elasticity of 191 GPa. The CFRP
149 bars have 30 mm diameter, tensile strength of 2400 MPa and a modulus of elasticity of 270
150 GPa. The SFRC developed in a parallel research has a compressive strength of 64 MPa (f_{cm})
151 and tensile strength of 6.77 MPa (f_t), with modulus of elasticity of 42.15 GPa (E_{cm}) obtained
152 through experimental tests. The influence of fibre orientation on the post-cracking behaviour

5

153 of SFRC was assessed by performing three point notched beam bending tests with series of
154 specimens for fibre orientation intervals [0-15°[, [15-45°[, [45-75°[and [75-90°]. By inverse
155 analysis of the obtained results, the quadri-linear tensile softening diagram shown in Fig. 5a
156 was obtained to model the fracture mode I propagation of the SFRC (presented in Table 2 of
157 section 4.2, Abrishambaf *et al.* 2015). For the present simulations, the fibres are considered to
158 have the best orientation towards the crack planes formed in the tower, which obliges
159 appropriate casting technology for assuring preferential orientation of fibres in the longitudinal
160 axis of a ring. However, the influence of fibre orientation on the response of the tower is
161 assessed in a parametric study described in section 4.2. Due to relatively low compressive strain
162 level in the installed SFRC rings with high compressive strength, it is assumed to behave in the
163 elastic stage of the compression regime. The tension and compression behaviour of steel
164 reinforcement (cables and connectors) is simulated by the stress-strain diagram represented in
165 Fig. 5b. More details of the models for the FRC and reinforcements can be found in [11] and
166 in [12], while the constitutive law of the interface finite elements is described in [13]. In the
167 current analysis, the interface elements are assigned the following properties: slip at the end of
168 the linear bond-slip relationship is 0.5 mm (S_0), slip at the peak bond stress is 2.5 mm (S_m),
169 material cohesion of 1 MPa, friction angle as 37°, parameter defining pre-peak bond stress-slip
170 relation is $\alpha_1=1$, parameter defining post-peak bond stress-slip relation $\alpha_2=1$ and a normal
171 stiffness (K_n) of 2.0×10^7 N/mm.
172

(a)

(b)

(c)
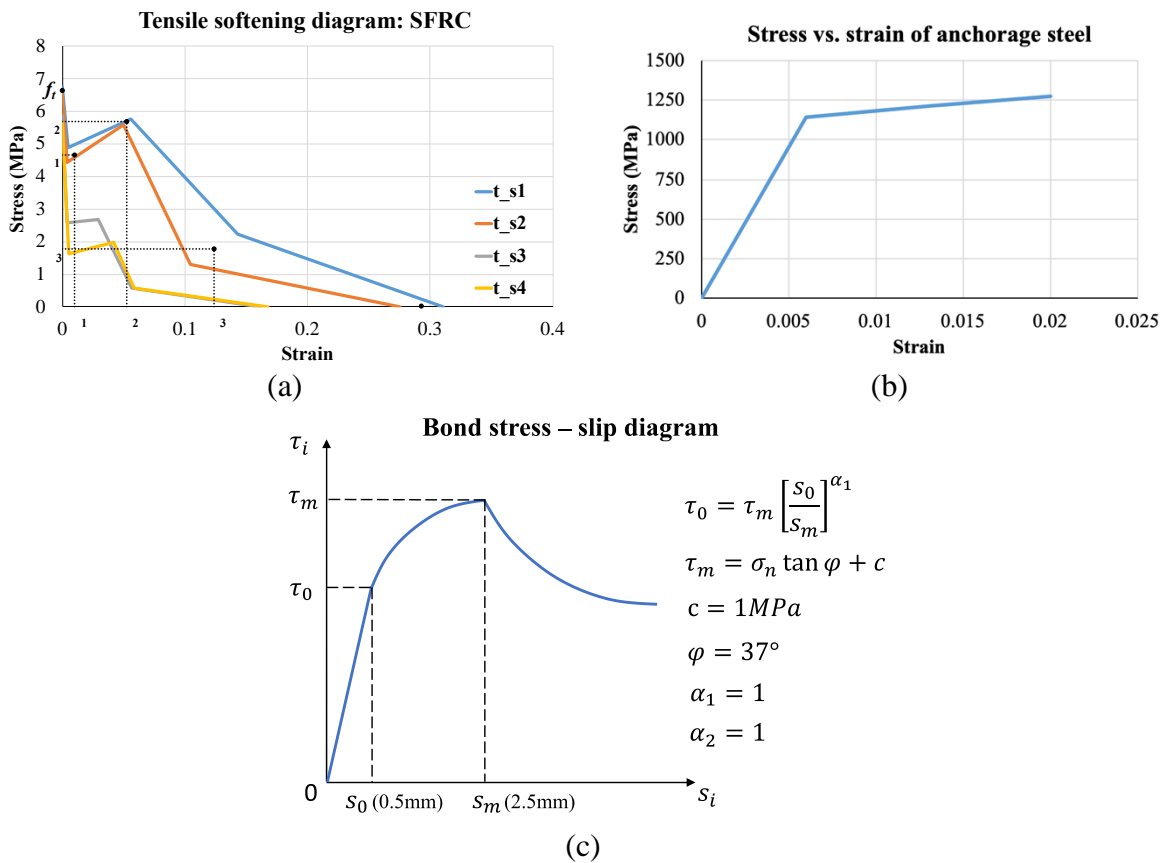
173 Fig. 5. Numerical model: (a) Tensile strain softening diagram for SFRC with different orientation
174 profiles; (b) Stress-strain diagram of the steel cables and connectors (c) Interface bond stress-slip
175 diagram

6

4. Results

4.1. Simulations of the Model 't_s1'

The loads acting on the global model are transmitted to the stiff loading plate placed on top part of the analysed model, shown in Fig. 3b, whose equivalent force and moments are shown in Table 2, factored according to Eq. (3).

Table 2. Different loads considered for the analysis

| Load description (Force/ Moment)	Notation	Values (kN/ kN·m)	Model
Self-weight	w_g	- (calculated by software)	
Wave and water current load	f_M	10171 kN (0-10m) 15946 kN (10-11m) 17821 kN (11-12m) 25921 kN (12-16.5m)	
Self-weight from above + dead weight of the rotor + nacelle	F_{zt}	6513 kN	
Wind force (f_w) + force due to the wind passing throughout the rotor + horizontal force by wave and water current	F_{xt}	1869 kN	
Moment due to wind force + moment due to wind generated by rotor + moment due to rotor + moment due to wave and water current	M_{yt}	155404 kN·m	
Torsional moment due to rotor	M_z	1789 kN·m	

The force *vs.* displacement of the "t_s1" model in X-direction is shown in Fig. 6a, where the displacement is measured on the top central node of the steel loading plate and the force as the summation of reaction forces at the base. Fig. 6b and 6c present the crack pattern at the end of the analysis (100% of F_x), on the bottom and top rings, respectively, where the maximum crack width is 0.18 mm, which was obtained by multiplying the maximum crack normal strain to the crack bandwidth of the integration point where it is being evaluated.
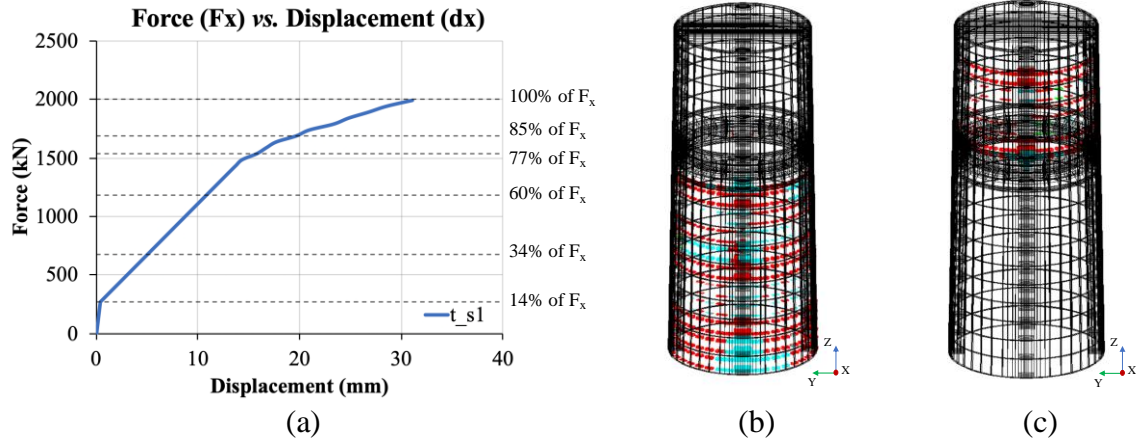
Fig. 6. (a) Force vs. Deflection; Crack pattern: (b) bottom ring and (c) top ring, model "t_s1" (crack status: opening in red colour; reopening in cyan colour).
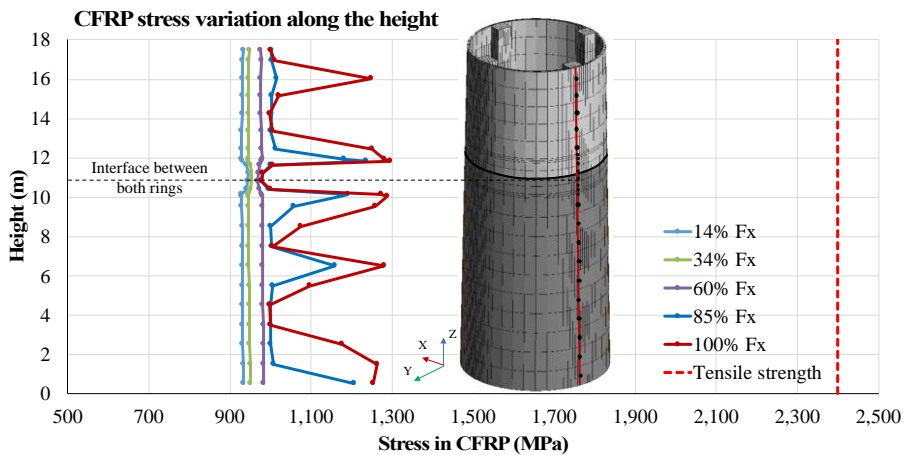
Fig. 7 shows the evolution of the stresses along the height of the tower in the post-tensioned steel cables (Fig. 7a), in the steel connectors (Fig. 7b) and in the pre-stressed CFRP bars (Fig. 7c) at different IP (black dots on the tower) for the indicated load levels (represented in Fig. 7). Each steel connector is simulated by a single element with 5 integration points, connecting two elements of SFRC (top and bottom ring). At the interface, the steel cables are connected by the first point of the element in ring 1 (bottom) and the second point of the element in ring 2 (bottom), simulating the continuity. Post-tensioned stresses of 60% of the yield stress were introduced in both the steel connectors and steel cables. According to the results, the maximum tensile stress in the post-tensioned steel cables and connectors did not attain the corresponding yield stress (1147 MPa). Similarly, in the CFRP reinforcement a maximum stress of 1290 MPa is reached i.e., 54% of the tensile strength (2400 MPa) of the respective CFRP bar. Stress jumps are obtained at certain IP at later stages due to crack formation (after 77% of F_x), as can be derived from Fig. 6b and 6c. At the interface between the two rings, no stress jump has occurred, which is a consequence of the effective anchorage of the steel connectors (Fig. 6b) and concrete-concrete interlock mechanism. This indicates that the post-tensioned steel cables are not necessary and the CFRP bar diameter can be reduced or even replaced by GFRP/Basalt bars, which faster significantly the costs and process of assembling the SFRC rings.

8

(a)

(b)

211
212

(c)
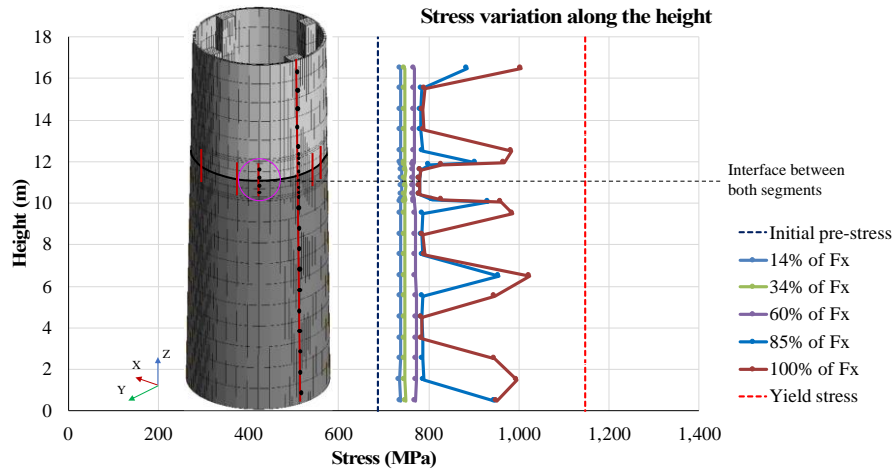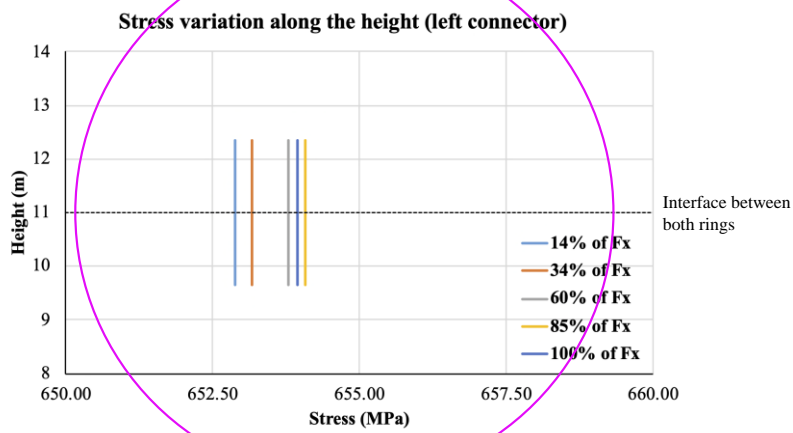
213   Fig. 7. Evolution of the stress field in the: (a) post-tensioned steel cables; (b) post-tensioned steel
214   connectors and (c) pre-tensioned CFRP bars, for different load combinations, model "t_s1".

215
216   Fig. 8 shows the stress distribution in Z-direction (vertical) from two different views at the end
217   of the analyses, 100% F_x. The combination of forces and moments applied on the current model

218 according to DNV for the considered combination (max. ULS: *F=1.0G+1.35E*), generate
219 tensile stresses (positive values, maximum of 100% of f_t) on one half of the tower and
220 compressive stresses (negative values, maximum of 58% of f_{cm} on the other half, which justify
221 the option for assuming linear behaviour for the SFRC in compression) on the other half. The
222 maximum shear stress variation on the interface layer between the two rings is lesser than 1.9
223 MPa (Fig. 8b).
224
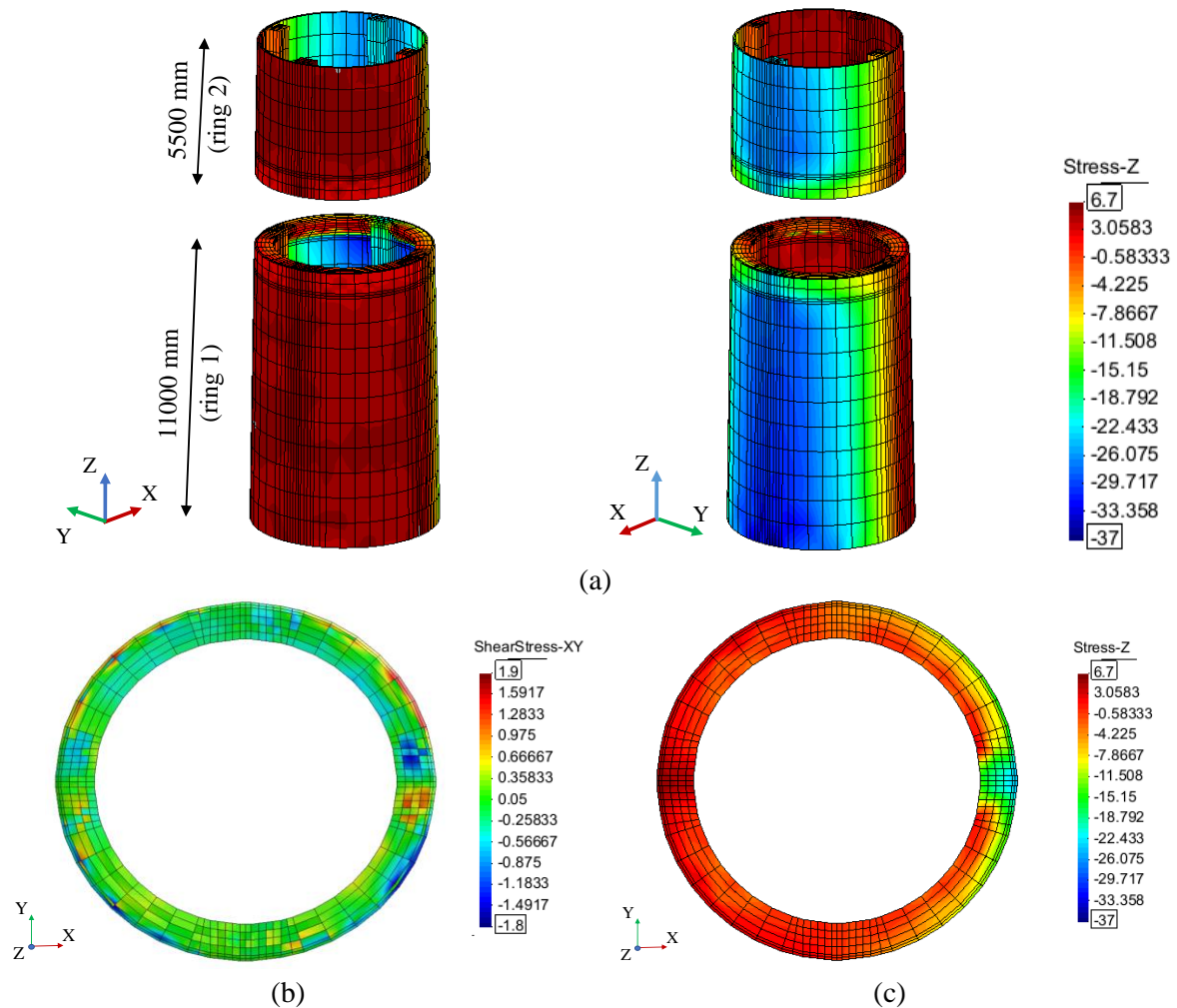
225 Fig. 8. Model "t_s1": (a) Z-stress field; (b) shear stress field (interface layer) and (c) Orthogonal
226 stresses interface layer) (all values are in MPa).

227

4.2. Parametric analyses

229 Parametric studies are performed to assess the influence of the connection between the rings
230 on the following aspects:
231   (a) SFRC fracture parameters, which are dependent on the fibre orientation;
232   (b) Pre-stress level in the steel (cables and connectors) and CFRP reinforcement;
233   (c) Shape of concrete-concrete interlock mechanism;
234   (d) Friction angle of the concrete-concrete contact conditions;
235   (e) Cohesion of the concrete-concrete contact conditions.
236

4.2.1. SFRC fracture parameters

The post-cracking tensile capacity of SFRC depends significantly on the fibre orientation towards the crack crossing the fibres [10]. This influence was investigated experimentally for four different casting conditions of SFRC in order to promote different fibre orientation profiles and, consequently, different fracture mode I parameters, whose corresponding values, define the quadrilinear diagram represented in Fig. 5a, and indicated in Table 3 [10].

Table 3. SFRC fracture parameters defining a quadrilinear tensile stress – strain softening diagram for four distinct fibre orientation profiles

Model	β	α_1 [-]	α_2 [-]	α_3 [-]	ξ_1 [-]	ξ_2 [-]	ξ_3 [-]	f_{ct} [MPa]	$G_{F,I}$ [N/mm]
t_s1	0°-15°	0.72	0.85	0.33	0.014	0.18	0.46	6.77	6.00
t_s2	15°-45°	0.68	0.86	0.20	0.014	0.18	0.38	6.50	5.10
t_s3	45°-75°	0.44	0.46	0.10	0.024	0.18	0.35	5.85	2.70
t_s4	75°-90°	0.29	0.35	0.10	0.032	0.25	0.35	5.64	2.70

Fig. 9a shows the results of force *vs.* displacement for the four toughness classes of SFRC. It is verified that, after crack initiation, the load carrying capacity of the tower increases with the post-cracking tensile capacity provided by the most favourable fibre orientation profiles. However, the difference on the load carrying capacity is small for fibre orientation profiles up to 45°. More favourable fibre orientation profiles promote the occurrence of more diffuse crack patterns, but of smaller width (Fig. 10).

(a)   (b)
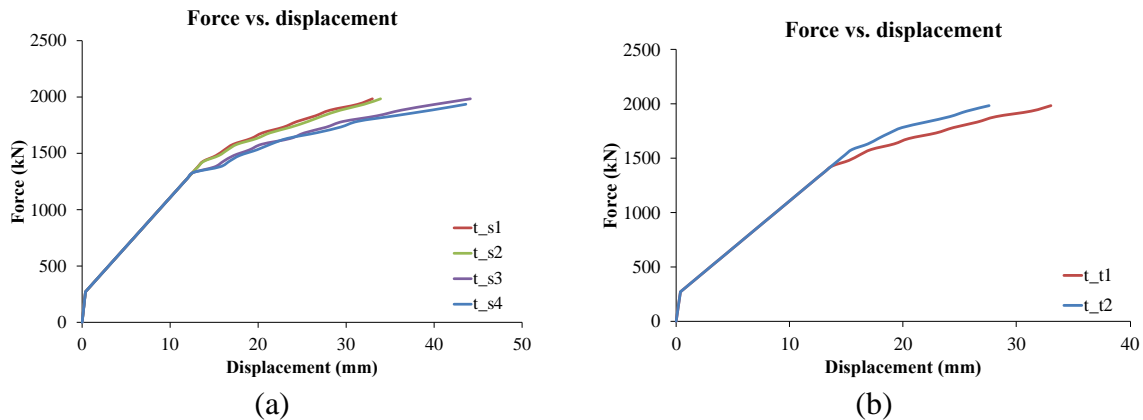
Fig. 9. Influence on the force-deflection response of the simulated model of the: (a) post-cracking tensile capacity of SFRC (due to preferential fibre orientation profile); (b) pre-stress level on steel and CFRP reinforcements.

(a) (b) (c) (d)
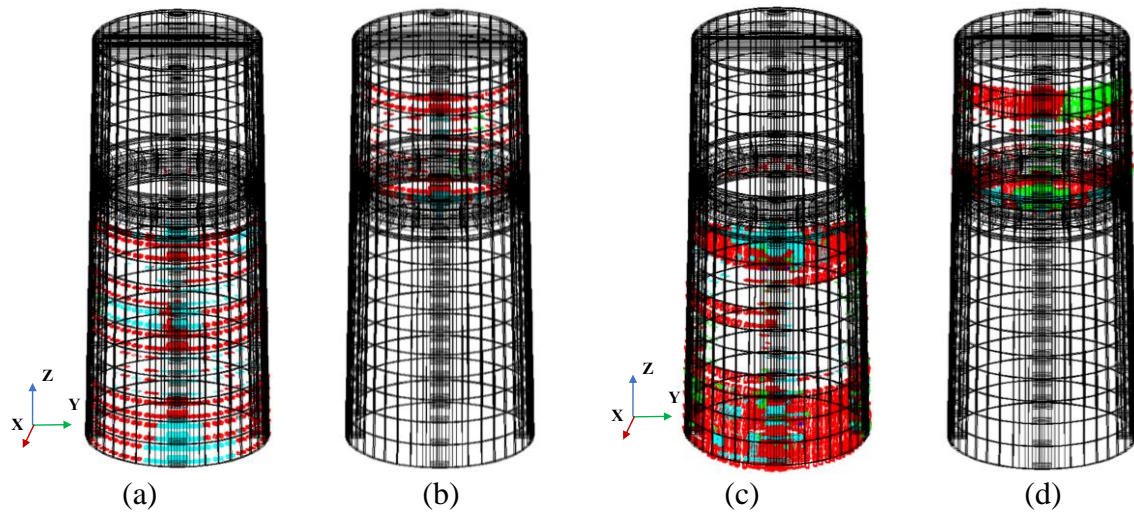
Fig. 10. Crack pattern: (a) Lower ring and (b) Upper ring of 't_s1'; (c) Lower ring and (d) Upper ring of 't_s4' (crack status: opening in red colour; closing in green colour, reopening in cyan colour).

4.2.2. Pre-stress level in the steel and CFRP reinforcements

Table 4 presents the two analysed pre-stress scenarios (percentage of the yield stress in case of steel and percentage of the tensile strength in case of CFRP) for the steel and CFRP reinforcements. The force *vs.* deflection for both the towers are shown in Fig. 9b, where it is verified as expected, the load at crack initiation, as well as in the post-cracking stage, decreases with the increased prestress level. At a deflection of 27.6 mm, the pre-stress scenario corresponding to the 't_t2' provided an increase of tower's load carrying capacity of 5.35% regarding the pre-stress scenario 't_t1', which was due to the lower number of cracks of smaller crack width in the 't_t2' (see Fig. 11).

Table 4. Adopted pre-stress percentage of the yield stress of the steel (cables and connectors) and CFRP reinforcement.

Type of Reinforcement	't_t1'		't_t2'	
	Pre-stress percentage (%)	Pre-stress (MPa)	Pre-stress percentage (%)	Pre-stress (MPa)
Steel	60	756	75	945
CFRP	40	960	60	1440

12

(a)   (b)   (c)   (d)
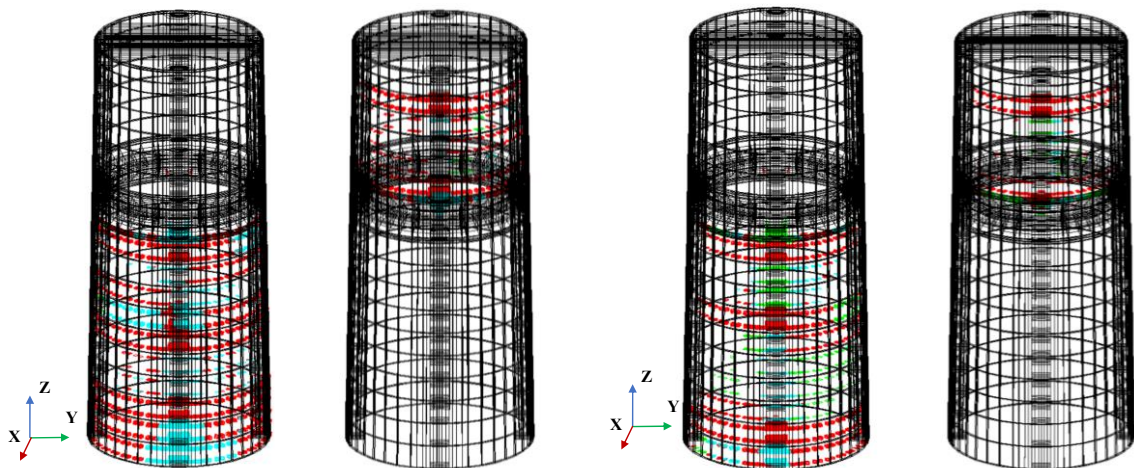
Fig. 11. Crack pattern: (a) Lower ring and (b) Upper ring of 't_t1'; (c) Lower ring and (d) Upper ring of 't_t2' (crack status: opening in red colour; closing in green colour, reopening in cyan colour).

4.2.3. Shape of concrete-concrete interlock mechanism

Two different geometric connections are examined to study the influence of inclinations on the contact faces of two adjacent SFRC rings. The first connection is inclined at 2° inward angle and 12° outward angle as shown in Fig. 12a, while the second is a planar contact, i.e., no interlock mechanism is provided (Fig. 12b). All the other geometric and material properties, and loading conditions are maintained the same in both cases.


(a)   (b)
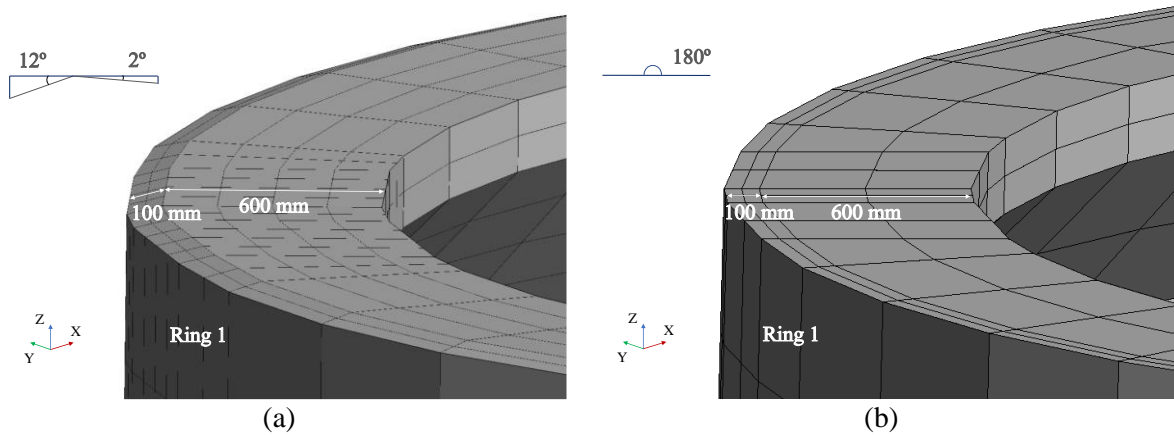
Fig. 12. Models with (a) and without (b) interlock mechanism in the concrete-concrete contact of two adjacent SFRC rings.

Fig. 13a shows the force *vs.* displacement of the models, with and without interlock mechanism at the concrete-concrete contact of two consecutive SFRC rings. It is verified that the interlock mechanism increases the tower load carrying capacity in the post-cracking stage of about a constant 3.5% with respect to the corresponding planar contact tower. The interlock shear resisting mechanism provided by the non-planar contact has decreased the stress level in the steel connectors (Fig. 13b). These favourable aspects provided by the non-planar concrete-concrete contact may be potentiated by optimizing the geometry of these contacts.


(a)   (b)
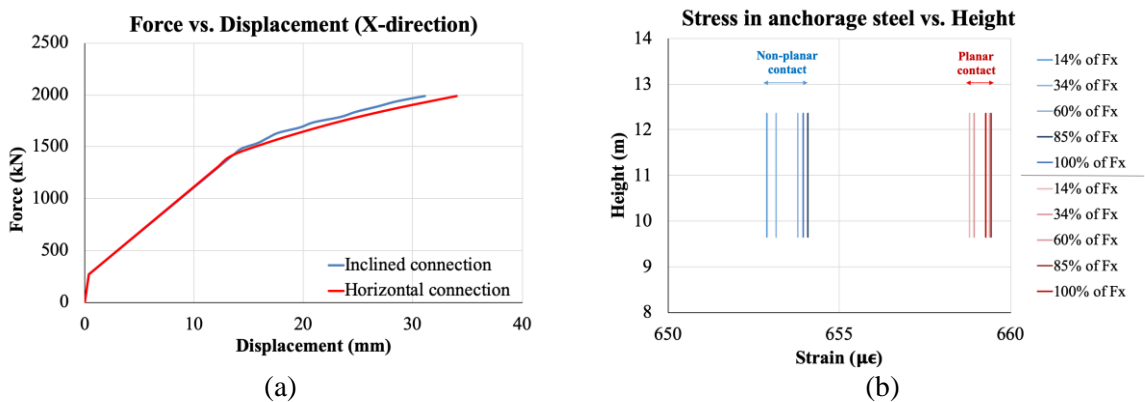
Fig. 13. Influence of the concrete-concrete contact geometry on the (a) force *vs.* displacement and (b) stress level on the steel connectors during the loading process.

13

297

298 The crack pattern of these simulations at 100% F_x (1989 kN) are presented in Fig. 14a and 14b
299 for the non-planar and planar contact conditions, respectively. It is verified the formation of
300 higher number of cracks in the planar contact conditions in both upper and lower rings, with
301 larger maximum crack width (0.25 mm over 0.19 mm). This is due to the larger displacement
302 of planar contact model, as a result of which the tower is subjected to higher stresses and more
303 cracks. In case of non-planar contact model, the additional shear resistance provided by the
304 inclination reduces the deformation and cracks with respect to planar contact model.

305

(a)   (b)
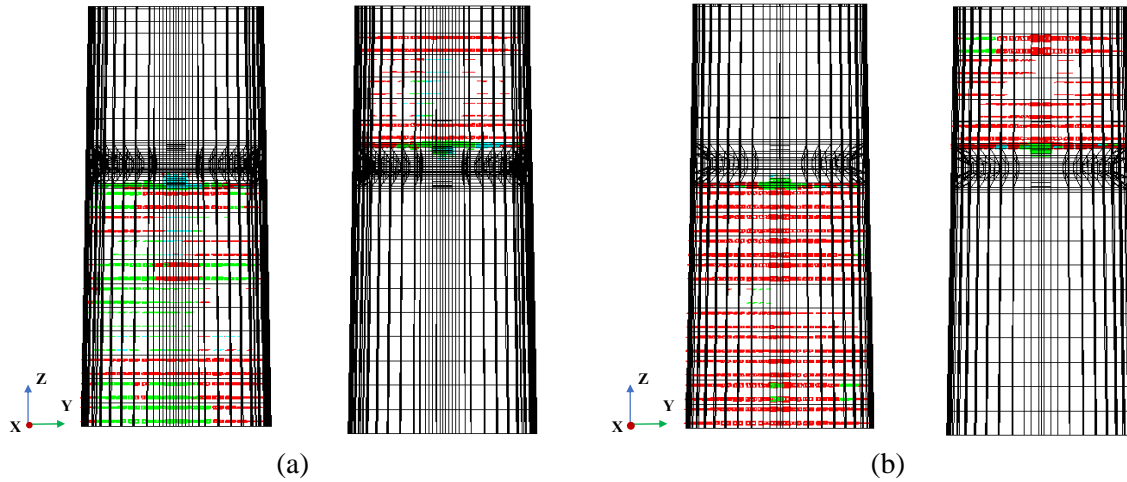
306 Fig. 14, Crack pattern for concrete-concrete (a) non-planar, and (b) planar, contact conditions (crack
307 status: opening in red colour; closing in green colour, reopening in cyan colour).

308

4.2.4. Friction angle of the concrete-concrete contact conditions

310 The influence of friction angle on the concrete-concrete contact conditions simulated through
311 the constitutive law of the interface FE is analysed by adopting the values presented in Table
312 5, while maintaining the same values for the other parameters. In the first two simulations, the
313 friction angle is varied with 0° and 37°, and a constant normal stiffness of 2×10^7 N/mm. With
314 this relatively high normal stiffness, the influence of the friction angle on the relevant
315 behavioural aspects of the tower is negligible (Fig. 15: model 't_a1' and 't_a2'), since sliding
316 is almost null regardless of the friction angle (Fig. 16a, b). However, reducing the normal
317 stiffness to 2×10^4 N/mm, the influence of the friction angle is already significant (model 't_a3'
318 and 't_a4' in Table 5), since a maximum variation of sliding between the two analysis was
319 2.5% and with respect to 't_a1' is 9.4% ('t_a3') and 6.7% ('t_a4'). The last two analysis in
320 Table 5, are performed with very low normal stiffness of 2×10^2 N/mm, where the models have
321 very large displacements and are almost distorted.

322

323 Table 5. Analysis for assessing the influence on the tower's behaviour of the friction angle and normal
324   stiffness of the concrete-concrete contact.

Model	Friction angle, θ (degrees)	Stiffness, K_n (N/mm)	Cohesion, C (MPa)	Remarks
t_a1	37°	2×10^7	1	Runs 100% of F_x, no slip between rings are observed
t_a2	0°			Runs 100% of F_x, no slip between rings are observed

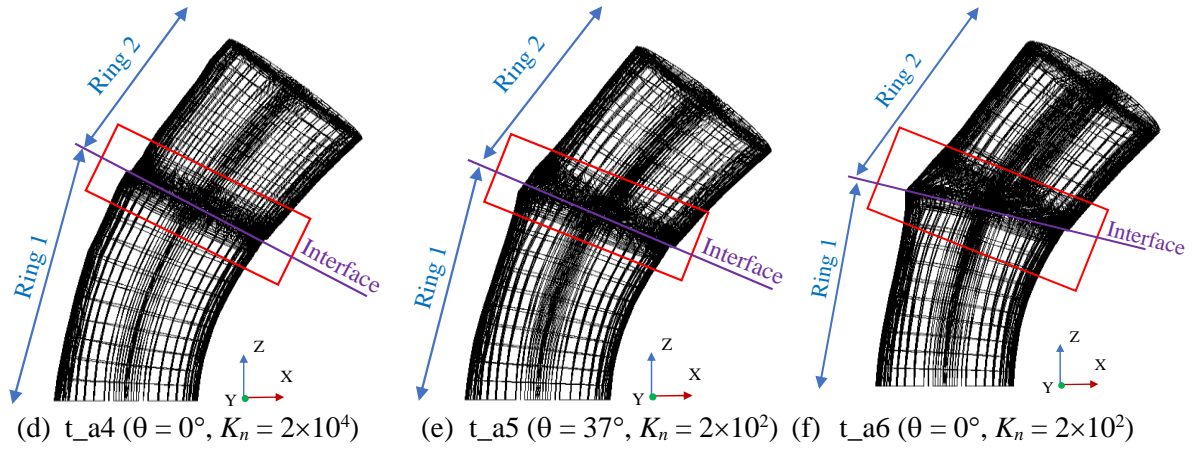|				
t_a3	37°	2×10⁴		Runs 100% of F_x, slip between rings are observed
t_a4	0°			Runs 100% of F_x, slip between rings are observed
t_a5	37°	2×10²		Runs up to 59% of F_x, slip between rings are observed and the analysis fails to converge
t_a6	0°			Runs up to 70% F_x, slip between rings are observed and the analysis fails to converge

The force *vs.* deflection of all these analyses are presented in Fig. 15, where the models with high stiffness (2×10⁷ N/mm) had almost no influence in the global response. The models with low stiffness (2×10⁴ N/mm) increased the overall deformation by 5.6% and 3.8%, and the last two analysis with very low stiffness (2×10² N/mm) even failed to complete the analysis, due to large displacements. These analyses shows the impact on the response of the tower, for the variation of friction angle which is dominant only for lower values of stiffness.
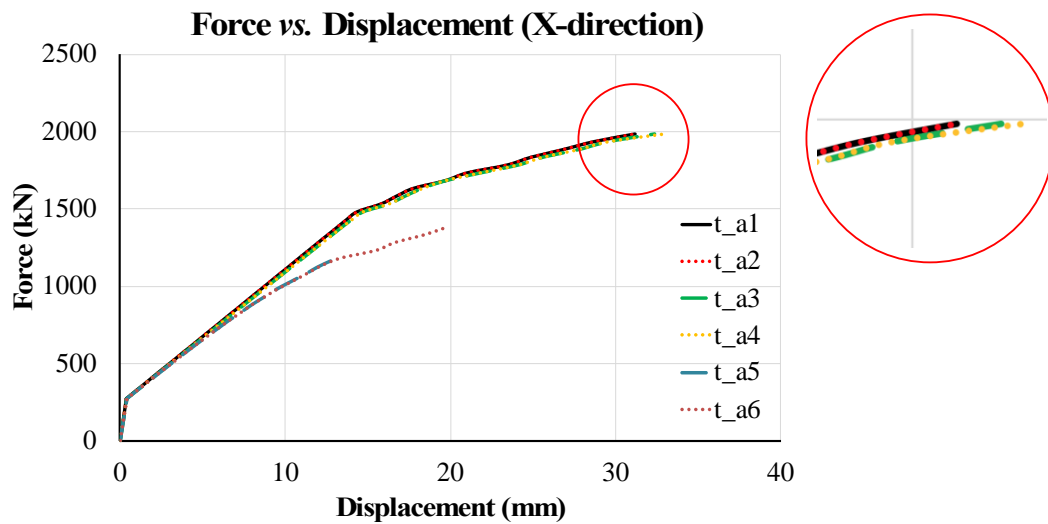
Fig. 15. Force *vs.* displacement influence of friction angle on the concrete-concrete contact condition.

(a) t_a1 (θ = 37°, K_n = 2×10⁷) (b) t_a2 (θ = 0°, K_n = 2×10⁷) (c) t_a3 (θ = 37°, K_n = 2×10⁴)

(d) t_a4 (θ = 0°, $K_n = 2\times10^4$)   (e) t_a5 (θ = 37°, $K_n = 2\times10^2$) (f) t_a6 (θ = 0°, $K_n = 2\times10^2$)
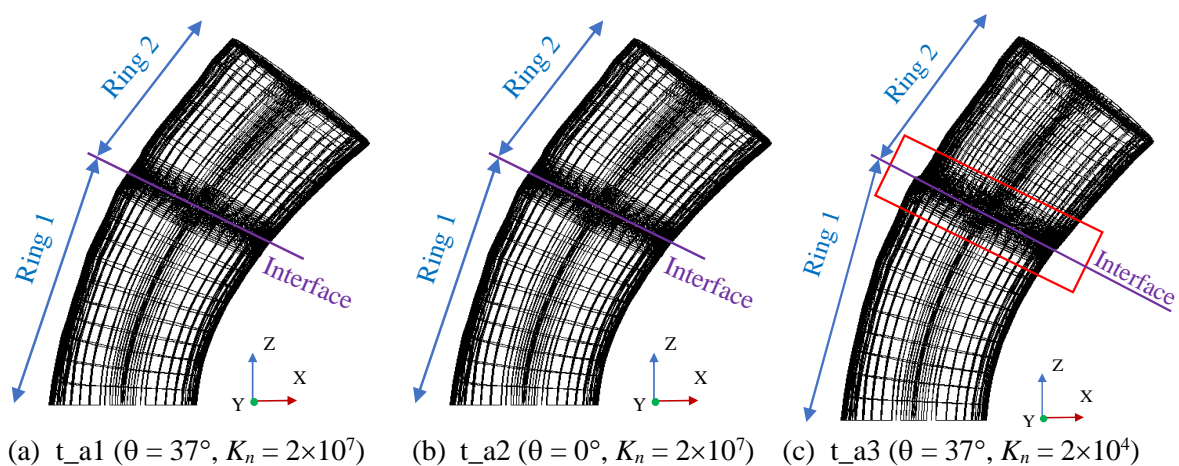
Fig. 16. Influence of the friction angle of the concrete-concrete contact on the deformation of models for normal stiffness of: (a)-(c) 2×10^7 N/mm, and (d)-(f) 2×10^4 N/mm.

4.2.5. Cohesion of the concrete-concrete contact conditions

The effect of the cohesion of the concrete-concrete contact conditions simulated through the constitutive law of the interface FE is analysed by adopting two values, 0 MPa and 1 MPa (the value recommended by *fib* Model Code 2010 [14]), while the remaining parameters are maintained the same. The analysis were grouped in three series in order to assess also the influence of the normal stiffness, as shown in Table 6.

Table 6. Analysis for assessing the influence on the tower's behaviour of the cohesion and normal stiffness of the concrete-concrete contact.

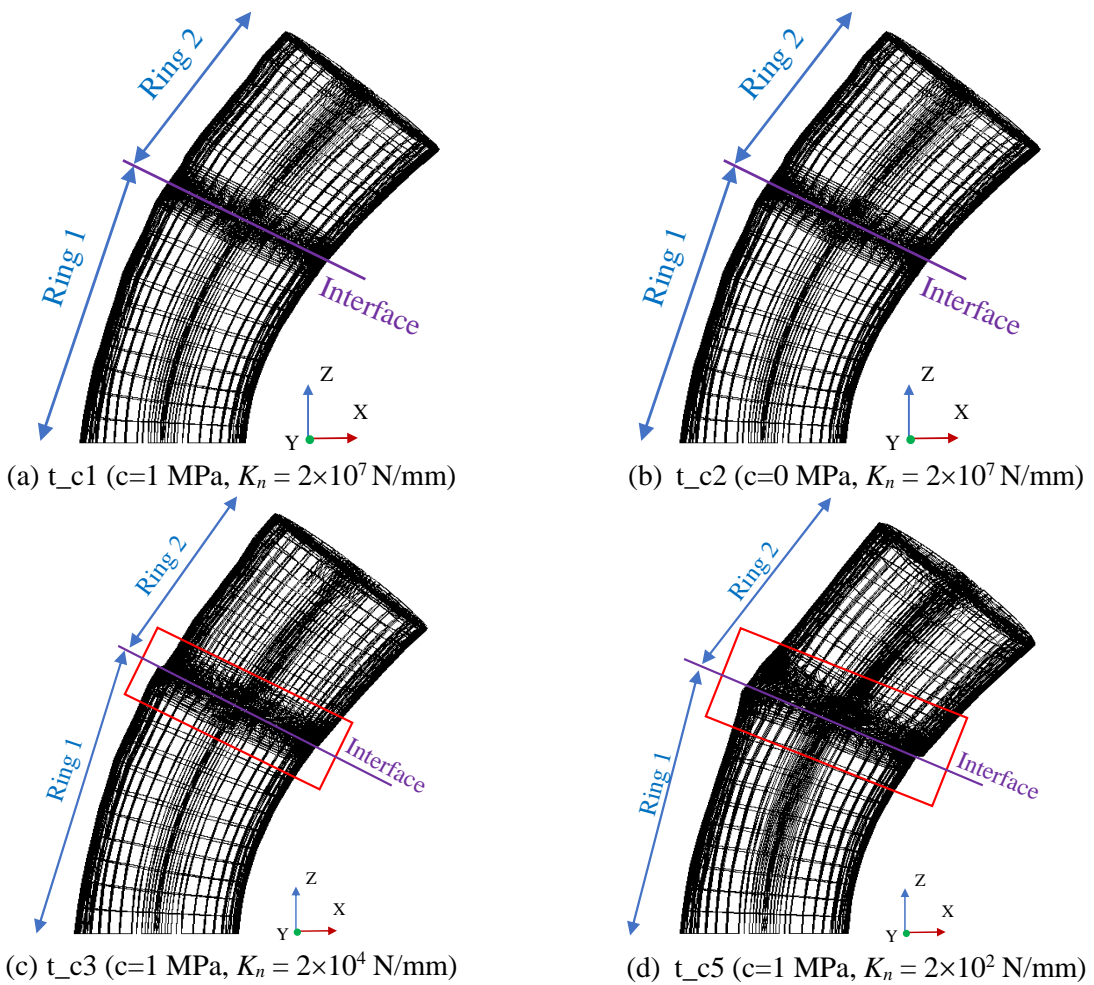| Model	Cohesion, C (MPa)	Stiffness, K_n (N/mm)	Friction angle, θ (degrees)	Remarks
t_c1	1	2×10^7	37°	Runs 100% of F_x, no slip between rings are observed
t_c2	0			Runs 100% of F_x, no slip between rings are observed
t_c3	1	2×10^4		Runs 100% of F_x, no slip between rings are observed
t_c4	0			Analysis fails to converge even the first load combination
t_c5	1	2×10^2		Runs up to 59% of F_x and fails to converge after, slip between rings are observed
t_c6	0			Analysis fails to converge even the first load combination

The first two models 't_c1' and 't_c2' with high stiffness (2×10^7 N/mm), has almost no influence on the structural performance of the towers, shown in Fig. 17 (force *vs.* displacement) and on the deformation plots where no slip is observed, Fig. 18(a, b). Reducing the stiffness to 2×10^4 N/mm in 't_c3' the overall deformation is increased by 5.6% and a slip of 1.01 mm takes place between the rings, Fig. 18c. However, further reducing the stiffness to 2×10^2 N/mm, the analysis of model 't_c5' stops at 59% of F_x, with an increased slip of 1.26 mm between the rings i.e., 24.7% increase with respect to 't_c3' (2×10^4 N/mm). The force *vs.* displacement graphs of all the models are shown in Fig. 17. Even though, the overall stiffness variation between 't_c1' and 't_c3' is not pronounced, the stiffness variation between 't_c1' and 't_c5' is quite drastic. In case of models 't_c4' and 't_c6' both the analysis fail to converge due to the

16

356 absence of cohesion, lower normal stiffness and higher displacement between the concrete-
357 concrete contact condition.
358
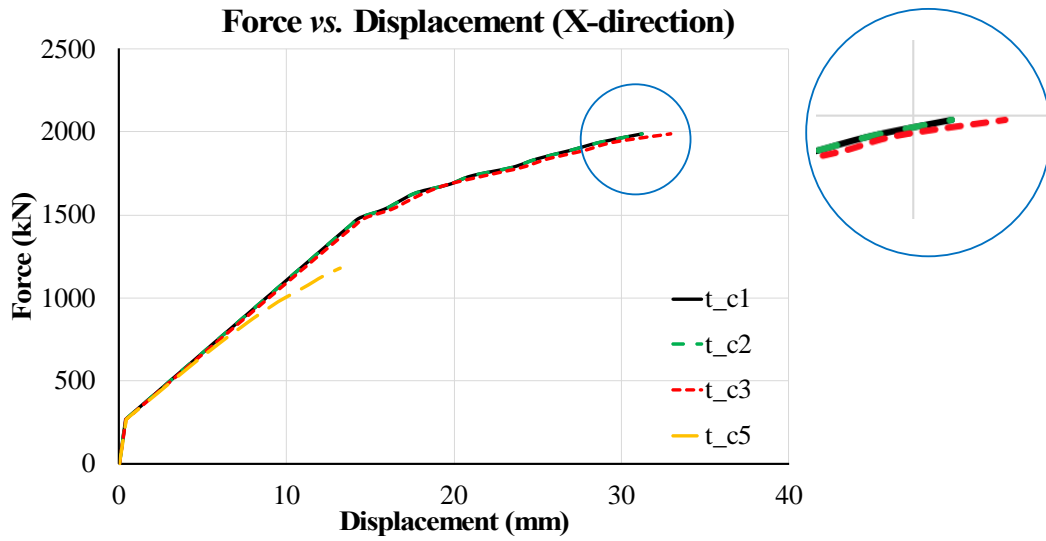
359 Fig. 17. Force *vs.* displacement influence on cohesion of concrete-concrete contact conditions.

360

(a) t_c1 (c=1 MPa, $K_n = 2\times10^7$ N/mm) (b) t_c2 (c=0 MPa, $K_n = 2\times10^7$ N/mm)

(c) t_c3 (c=1 MPa, $K_n = 2\times10^4$ N/mm) (d) t_c5 (c=1 MPa, $K_n = 2\times10^2$ N/mm)

361 Fig. 18 Deformation of models with different cohesive values.

17

362

5. Conclusions

The validation of the numerical work will be further explored in the next stages of the research after executing experimental work in the laboratory. According to the results obtained from the FE numerical analyses, the following conclusions are summarised:

- The proposed material-structural concept of offshore wind tower, combining SFRC, prestressed CFRP bars, post-tensioned steel cables, and post-tensioned steel connectors greatly reduces the wall thickness by 75%, with respect to conventional concrete construction;
- The structural behaviour of this tower was assessed by performing material nonlinear analysis and considering some of the most design governing loading conditions, having accomplished the most unfavourable combination for ULS;
- The maximum crack width obtained in the model with the SFRC of highest post-cracking tensile capacity (due to the consideration of fibre orientation) was 0.18 mm, for ULS conditions indicating that no corrosion problems is expected even by adopting steel fibres;
- None of the steel reinforcements have yielded nor they are closer to the yielding value, even though some variations are observed at crack locations, they are within the corresponding yield values;
- By managing the pre-stress level applied to the CFRP bars and steel strands, the stiffness of the response of the tower can be adapted;
- Inclined connection between the rings has better performance in terms of reduced stresses in the post-tensioned steel connectors, overall deformation and smaller maximum crack width;
- The influence of the friction angle and cohesion of the concrete-concrete contact conditions between consecutive SFRC rings has only a detrimental influence of the tower's behaviour if relatively small normal stiffness is assumed for the contact conditions.

Acknowledgements

References

[1] G. Giebel and C. B. Hasager, "An Overview of Offshore Wind Farm Design", in Ostachowicz W., McGugan M., Schröder-Hinrichs JU., Luczak M. (eds.) *MARE-WINT*, Springer, Cham, pp. 337-346, Denmark, 2016.

[2] GWEC, "GWEC Global Wind 2017 Report - A snapshot of top wind markets in 2017: Offshore wind", 2017.

[3] S. Malhotra, "Selection, Design and Construction of Offshore Wind Turbine Foundations", April, 2011.

[4] S. Malhotra, "Design and construction considerations for offshore wind turbine foundations", in *Proceedings of the International Conference on Offshore Mechanics and Arctic Engineering - OMAE*, vol. 5, pp. 635–647, January 2007.

[5] H. Ma, J. Yang, and L. Chen, "Numerical analysis of the long-term performance of

offshore wind turbines supported by monopiles", *Ocean Engineering*, vol. 136, pp. 94–105, May, 2017.

[6] F. P. Figueiredo, M. E. Hassanabadi, J. A. O. Barros, and A. Ventura-Gouveia, "Simplifed Design Approach of Offshore Wind Towers", *Report*, Department of Civil Engineering of the University of Minho, 2018.

[7] DNV, "DNV-OS-J101 Design of Offshore Wind Turbine Structures", *May*, May, pp. 212–214, 2014.

[8] F. P. Figueiredo, J. A. O. Barros, and A. Ventura-Gouveia, "Nonlinear Analysis of offshore Wind Towers in Prefabricated Segments of Prestressed Fibre Reinforced Concrete", In *RILEM SCC2020 - The third RILEM Spring Convention and Conference: ambitioning a sustainable future for built environment: comprehensive strategies for unprecedented challenges*, University of Minho, Guimarães, Portugal, 10-14 March, 2020.

[9] A. Ventura-Gouveia, J. A. O. Barros, A. F. M. Azevedo, and J. M. Sena-Cruz, "Multi-Fixed smeared 3D crack model to simulate the behavior of fiber reinforced concrete structures", *CCC2008-Challenges Civil Construction*, Torres Marques et al. (eds.), p. 11, Porto, Portugal, 16-18 April, 2008.

[10] A. Abrishambaf, J. A. O. Barros, and V. M. C. F. Cunha, "Time-dependent flexural behaviour of cracked steel fibre reinforced self-compacting concrete panels", *Cement and Concrete Research*, vol. 72, pp. 21–36, June, 2015.

[11] J. A. O. Barros, M. Breveglieri, A. Ventura-Gouveia, G. M. Dalfré, and A. Aprile, "Model to simulate the behavior of RC beams shear strengthenend with ETS bars", *VIII International Conference on Fracture Mechanics of Concrete and Concrete Structures – FraMCoS-8*, J.G.M. Van Mier, G. Ruiz, C. Andrade, R.C. Yu and X.X. Zhang (eds.), pp. 505–516, Toledo, Spain, 10-14 March, 2013.

[12] A. Ventura-Gouveia, "Constitutive models for the material nonlinear analysis of concrete structures including time-dependent effects", *PhD Thesis*, University of Minho, Guimaraes, Portugal, 2011.

[13] T. D. S. Valente, "Advanced numerical models for analysis of the behaviour of structures strengthened with an innovative technique", *PhD Thesis*, University of Minho, Portugal, 2019.

[14] fib CEB-FIP, "fib Model Code for Concrete Structures 2010", *Wilhelm Ernst & Sohn*, 2010.